

# Oxidation of Levitated *exo*-Tetrahydrodicyclopentadiene Droplets Doped with Aluminum Nanoparticles

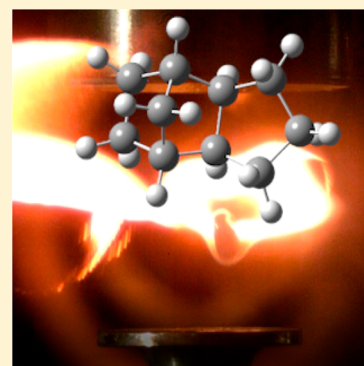
Michael Lucas,<sup>†,§</sup> Stephen J. Brotton,<sup>†,§</sup> Ahreum Min,<sup>†</sup> Michelle L. Pantoya,<sup>‡,§</sup> and Ralf I. Kaiser<sup>\*,†,§</sup>

<sup>†</sup>Department of Chemistry, University of Hawai'i at Manoa, Honolulu, Hawaii 96822, United States

<sup>‡</sup>Mechanical Engineering Department, Texas Tech University, Lubbock, Texas 79409, United States

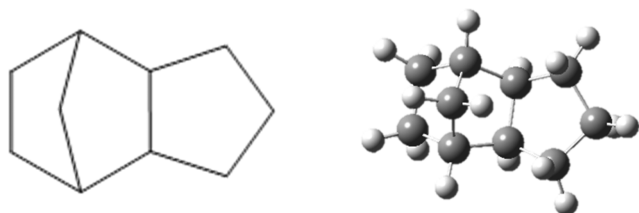
**S** Supporting Information

**ABSTRACT:** Advancement of the next generation of air-breathing propulsion systems will require developing novel high-energy fuels by adding high energy-density materials such as aluminum to enhance fuel performance. We present original measurements, obtained by exploiting the ultrasonic levitation technique, to elucidate the oxidation of *exo*-tetrahydrodicyclopentadiene (JP-10; C<sub>10</sub>H<sub>16</sub>) droplets doped with 80 nm-diameter aluminum nanoparticles (Al NPs) in an oxygen–argon atmosphere. The oxidation was monitored by Raman, Fourier-transform infrared (FTIR), and ultraviolet–visible (UV–Vis) spectroscopies together with high-speed optical and IR thermal-imaging cameras. The addition of 0.5 wt % of the Al NPs was critical for ignition under our experimental conditions occurring at 540 ± 40 K. Diatomic radicals such as OH, CH, C<sub>2</sub>, and AlO were observed during the oxidation of the doped JP-10 droplets, thus providing insight into the reactive intermediates. The influence of the Al NPs on the reaction mechanism is discussed.



Air-breathing propulsion systems rely on the combustion of hydrocarbon fuels such as of Jet Propellant-10 (JP-10).<sup>1,2</sup> The *exo*-tetrahydrodicyclopentadiene molecule (C<sub>10</sub>H<sub>16</sub>; Scheme 1) represents the major component of JP-10 and is

**Scheme 1. Two-Dimensional Structure of the JP-10 Molecule (left); Stick-and-Ball Model of the Molecular Structure of JP-10 (right)**<sup>a</sup>



<sup>a</sup>Carbon and hydrogen atoms are color-coded in gray and white, respectively.

defined by a high volumetric energy (39.6 kJ cm<sup>-3</sup>) due to three five-membered ring moieties incorporated into a single molecule along with the inherent ring strain energy. This makes JP-10 not only an attractive fuel for missiles, pulse-detonation engines, and ramjets,<sup>1,3,4</sup> but also interesting for the physical (organic) chemistry, combustion, and theoretical chemistry communities to explore its decomposition and oxidation experimentally, theoretically, and in combustion models.<sup>5–11</sup> Exploiting shock tubes,<sup>10</sup> flow tubes,<sup>7,12–14</sup> and high-temperature chemical reactors,<sup>5,6,15</sup> a detailed understanding of the decomposition of pure JP-10 is beginning to emerge. The unimolecular decomposition (“pyrolysis”) of JP-

10 leads to smaller hydrocarbon molecules and reactive transient species, among them aliphatic radicals, resonantly stabilized free radicals (RSFRs), and aromatic radicals (ARs),<sup>5,6</sup> which initiate the complex chemistry in the oxidation of JP-10 based jet fuel. This initial decomposition chemistry, which is temporarily uncoupled from the oxidation stage,<sup>16</sup> is often dubbed as “delivering the building blocks” for the oxidation of JP-10.

However, concerns on the limited volumetric energy density of traditional hydrocarbon fuels of up to only 40 kJ cm<sup>-3</sup>, which severely constrain the range and hence performance of air-breathing propulsion systems, are growing. Consequently, advanced next generation air-breathing propulsion systems require the development of fuel with higher energy per unit volume and molecular weight compared to traditional hydrocarbon fuels. This necessitates development of the next generation of high energy-density fuel and high energy-density fuel additives ultimately to enhance the performance and range of air-breathing propulsion systems. A key approach to increase the energy density of the liquid fuel is to include solid particle additives such as high energy-density nanoparticles (NPs).<sup>17,18</sup> Aluminum (Al) holds an energy density of 84 kJ cm<sup>-3</sup>;<sup>17</sup> aluminum NPs have consequently generated intense interest as a high energy fuel additive, since the addition of aluminum NPs has the unique potential of improving the performance of hydrocarbon fuels including JP-10.<sup>19–29</sup> The addition of Al NPs has been shown to improve the performance of JP-10. E

**Received:** July 31, 2019

**Accepted:** September 9, 2019

**Published:** September 9, 2019



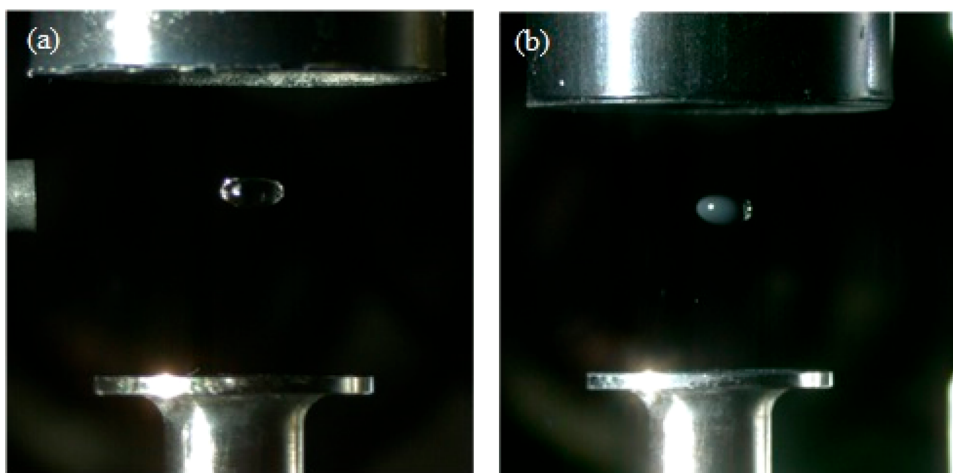


Figure 1. Photographs of levitated droplets of (a) pure JP-10 and (b) Al/JP-10 levitated in argon.

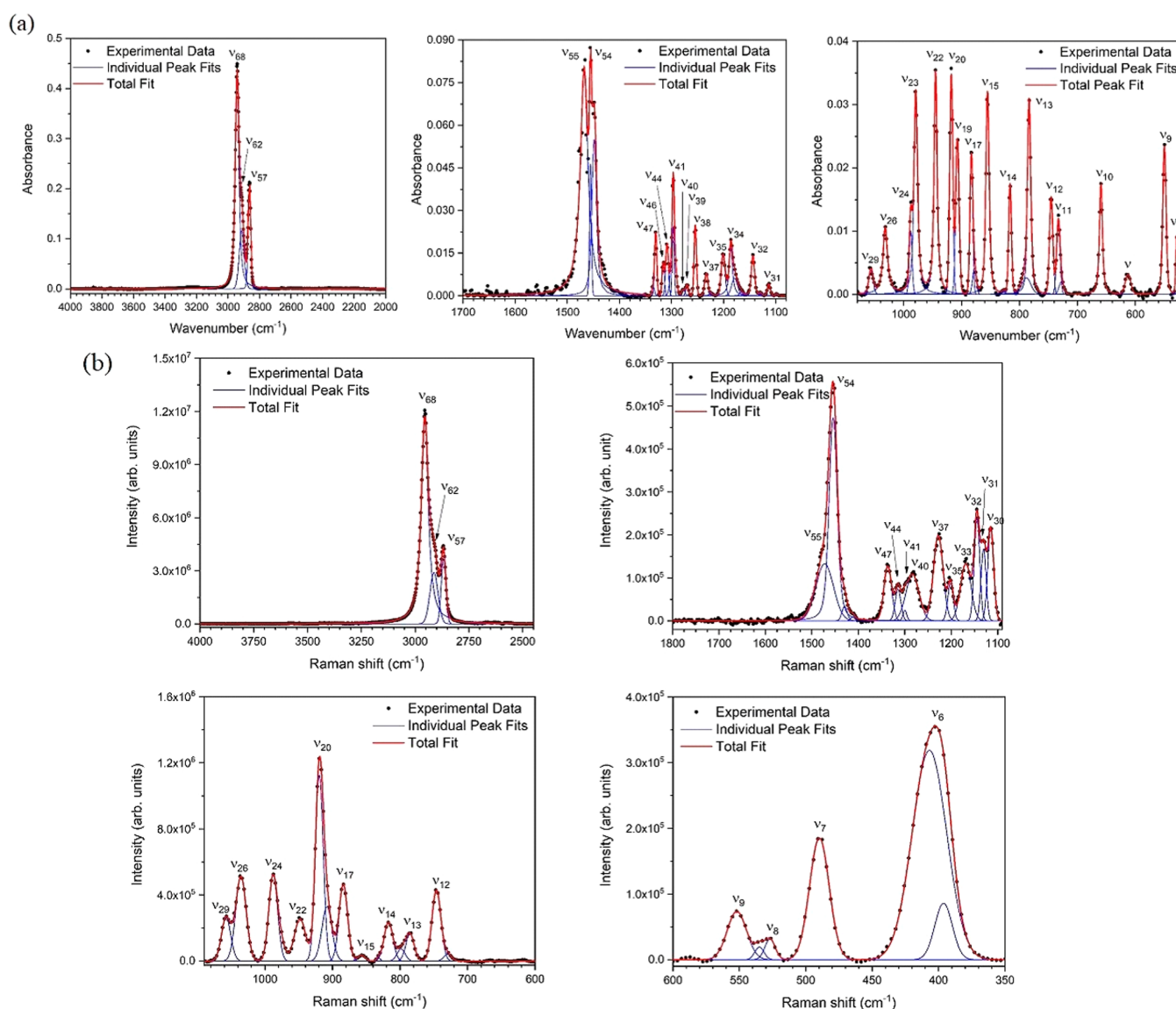


Figure 2. (a) FTIR and (b) Raman spectra of pure JP-10. Individual peaks are labeled with  $\nu_6$ – $\nu_{68}$ , and the peak assignments are compiled in Table S1.

et al. demonstrated that adding Al NPs increased the volumetric energy of JP-10 by 10%, shortened the ignition

delay times, and increased burn times in the combustion process.<sup>22,23</sup> Luo et al. exploited a small-scale reactor to study

the combustion of JP-10 containing 30–50 nm diameter Al NPs<sup>27</sup> and found that the aluminum-doped samples resulted in nearly 10% higher combustion efficiency than pure JP-10 samples. Chen et al. and Liu et al. exploited a laser ignition system to study the combustion of droplets of JP-10 and JP-10 doped with 80 nm-diameter Al NPs suspended on a silicon carbide (SiC) fiber.<sup>24,25</sup> Chen et al. reported that the combustion of a droplet containing 10 wt % NPs reached a maximum temperature of 2116 K with a combustion efficiency of over 99%.<sup>24</sup> Liu et al. suggested the following mechanism for the ignition and combustion processes of JP-10 droplets containing Al NPs.<sup>25</sup> Liquid JP-10 burns during the early stages of droplet combustion followed by Al combustion in the later stages, since the oxidation of JP-10 consumes oxygen on the surface of the droplet and, hence, creates a local oxygen deficiency within the droplet that prevents the Al from reacting. As the JP-10 is consumed, the heating causes the surface Al oxide shell of some NPs to break and therefore small droplets of Al are ejected in a micro-explosion. After the JP-10 is consumed, oxygen becomes available for Al combustion to begin within the droplet. However, these studies have not elucidated the chemical reaction mechanisms, intermediates, products, and branching ratios and how—on the molecular level—aluminum NPs influence the combustion properties of JP-10. This basic understanding of, for instance, the nature of the (radical) reaction intermediates, products, and rate constants and how these depend on important parameters (temperature, pressure, concentration of the additive, particle-size distribution, droplet size) is critical to develop predictive combustion models and ultimately to develop the next generation of air-breathing ramjet and scramjet systems with superior energy per unit volume and molecular weight compared to traditional hydrocarbon fuels such as JP-10.

In this Letter, we present original experiments on the ignition and oxidation of a single droplet of JP-10 with and without 80 nm-diameter aluminum NPs. The JP-10 droplets doped with the Al NPs are henceforth denoted by Al/JP-10. The reactions were conducted by levitating a single droplet of JP-10 in an ultrasonic levitator, which is enclosed within a pressure-compatible process chamber interfaced to complementary Raman, ultraviolet–visible (UV–Vis), and Fourier-transform infrared (FTIR) spectroscopic probes (Experimental Methods).<sup>30–33</sup> The droplet is viewed by high-speed optical and infrared (IR) thermal-imaging cameras to monitor physical changes to the sample in real time including the droplet size and temperature. The heating of the droplet and ignition are performed by a carbon dioxide laser. The processing within an ultrasonic levitator allows us to study the oxidation of a single droplet in a container-less environment under well-defined chemical and physical conditions with complementary spectroscopic probes simultaneously monitoring the chemical changes of the sample *in situ*. The apparatus is thus ideally suited to investigate the dependence of the reactions on the aforementioned important experimental parameters.

Before the physical and chemical changes of JP-10 and Al/JP-10 droplets in the oxidation process were investigated, it was critical to record reference spectra of the unreacted JP-10 and Al/JP-10 droplets (Figure 1). A comparison of the unreacted reference spectra with measurements during and after the oxidation enables the newly formed peaks and bands to be identified. The FTIR and Raman spectra are displayed in Figure 2; assignments of the individual peaks are compiled in Table S1. The vibrational spectrum of JP-10 has not been

reported previously. Theoretical calculations<sup>5</sup> were therefore conducted to guide the vibrational assignments of JP-10 (Table S1). Briefly, the absorptions in the infrared spectrum can be divided into five regions. The highest wavenumber region of 2800–3200 cm<sup>-1</sup> is associated with CH and CH<sub>2</sub> stretching modes; for example,  $\nu_{57}$  and  $\nu_{68}$  at 2865 and 2942 cm<sup>-1</sup>, respectively, are associated with CH stretching, whereas  $\nu_{62}$  at 2913 cm<sup>-1</sup> is linked with CH<sub>2</sub> stretching. The central region of 1400–1600 cm<sup>-1</sup> includes the  $\nu_{54}$  and  $\nu_{55}$  scissoring modes of CH<sub>2</sub> at 1456 and 1468 cm<sup>-1</sup>, respectively. The 1000–1400 cm<sup>-1</sup> range reveals CH and CH<sub>2</sub> wagging and twisting modes with the wagging modes generally occurring at higher wavenumbers than the twisting modes. The CH wagging mode  $\nu_{41}$  is evident at 1297 cm<sup>-1</sup>, while peaks  $\nu_{29}$ ,  $\nu_{34}$ ,  $\nu_{40}$ ,  $\nu_{43}$ ,  $\nu_{44}$ , and  $\nu_{46}$  are caused by CH<sub>2</sub> wagging modes. The peaks labeled  $\nu_{20}$ ,  $\nu_{26}$ ,  $\nu_{30-32}$ ,  $\nu_{35}$ ,  $\nu_{38}$ , and  $\nu_{39}$  are associated with the CH<sub>2</sub> twisting modes. The wavenumber regions of 700–1000 and 400–700 cm<sup>-1</sup> are connected to the CC stretching ( $\nu_{12}$ ,  $\nu_{13}$ ,  $\nu_{17}$ ,  $\nu_{19}$ ,  $\nu_{23}$ ,  $\nu_{24}$ ) and CCC bending modes ( $\nu_9$ ,  $\nu_{11}$ ,  $\nu_{15}$ ), respectively. The 400–1000 cm<sup>-1</sup> region also contains the ring modes  $\nu_8$  at 528 cm<sup>-1</sup> (ring twisting),  $\nu_{10}$  at 659 cm<sup>-1</sup> (ring rocking), and  $\nu_{22}$  at 945 cm<sup>-1</sup> (ring breathing) in addition to a CH<sub>2</sub> rocking mode at 816 cm<sup>-1</sup> ( $\nu_{14}$ ). The Raman spectra are similar to the FTIR spectra in some spectral regions, but distinct differences arise at other wavenumbers owing to different selection rules for the two spectroscopic techniques.<sup>34</sup> The key differences include peaks  $\nu_{20}$  and  $\nu_{54}$  being more prominent and a decrease in intensities of peaks  $\nu_{22}$ ,  $\nu_{41}$ , and  $\nu_{55}$  in the Raman spectrum compared to the FTIR spectrum.

The addition of the aluminum NPs did not produce any new discrete peaks in the FTIR and Raman spectra (Figures S1 and S2). Instead, the aluminum NPs caused a broad background to appear in the FTIR spectrum from 500 to 1000 cm<sup>-1</sup>, which is produced by the Al–O stretching mode of the Al<sub>2</sub>O<sub>3</sub> molecules within the outer layer of the NPs.<sup>35–38</sup> Similarly, the addition of the Al NPs caused the Raman peaks to be superimposed on a broad, structureless continuum which resembles the spectra of amorphous Al<sub>2</sub>O<sub>3</sub>.<sup>39,40</sup> This amorphous solid is composed of aluminum oxides with different bond angles and lengths, which consequently produces vibrational modes with a large range vibrational frequencies, thus creating broad bands in the vibrational spectra.<sup>41</sup> The Al–Al lattice vibrations associated with the metal core occur at wavelengths below 400 cm<sup>-1</sup> and so are not observed in the region of the present Raman and FTIR spectra.<sup>42</sup>

After recording the reference spectra, we studied droplet oxidation. Droplets with typical dimensions of (2.7 ± 0.3) mm × (1.2 ± 0.3) mm were levitated in an oxygen–argon atmosphere at a pressure of 864 Torr. A carbon dioxide laser was used to heat and hence ignite the levitated droplet. The first step was to determine the conditions required to ignite a pure droplet of JP-10 by varying the percentage of oxygen in the chamber from 0 to 100% and the laser power. The ignition was monitored by a high-speed optical camera and an IR thermal-imaging camera to determine the ignition temperature. The pure JP-10 droplets were found not to ignite under any conditions, even when levitated in 100% oxygen and for the maximum laser power of 34 W. The JP-10 droplet reached a maximum temperature of 452 ± 10 K, which is below the autoignition temperature (509 K) and the boiling point (458 K) of pure JP-10,<sup>4</sup> before the heating of the gas around the

droplet caused it to fall out of the trap. However, the addition of only 0.5 wt % of 80 nm-diameter aluminum NPs caused the droplet to ignite in a 40% O<sub>2</sub> and 60% Ar gas mixture at a laser power of  $10 \pm 1$  W, and in a 30% O<sub>2</sub> and 70% Ar gas mixture at a laser power of  $30 \pm 2$  W. All further investigations on the oxidation of Al/JP-10 droplets were performed with a 40% O<sub>2</sub> and 60% Ar gas mixture at 864 Torr and at the higher laser power of  $21 \pm 2$  W to ensure that the droplet ignited on nearly 100% of attempts. The mean temperature required to ignite the Al/JP-10 droplets was determined to be  $540 \pm 40$  K.

To determine whether ignition is linked to the unoxidized aluminum within the NPs or the potential catalytic effects of the aluminum oxide (Al<sub>2</sub>O<sub>3</sub>) layer that surrounds the NPs with thicknesses of  $4 \pm 1$  nm,<sup>43</sup> experiments were conducted by adding 0.5 wt % of Al<sub>2</sub>O<sub>3</sub> NPs to JP-10 (Figure S3). The droplets containing the aluminum oxide reached a maximum temperature of  $445 \pm 8$  K and did not ignite, and therefore ignition of the Al/JP-10 droplets was not initiated by surface catalysis on aluminum oxides. Al/JP-10 droplets are dark at visible wavelengths (Figure 1) and consequently might ignite only because of the resulting increased absorption of heat from the infrared laser. To test this hypothesis, we doped JP-10 with 0.5 wt % of copper oxide (CuO) NPs, which produced droplets with a similar dark appearance as the Al/JP-10. However, the CuO-containing droplet did not ignite and reached a maximum temperature of only  $443 \pm 8$  K before ejection from the trap, which is significantly lower than the Al/JP-10 maximum temperature of 540 K. At present, the CuO measurements therefore do not enable us to exclude the possibility that increased absorption at the laser wavelength of 10.6 μm, rather than at visible wavelengths, caused the Al/JP-10 droplet to ignite.

After the optimum ignition conditions for the Al/JP-10 droplets were determined, the ignition process was monitored with high-speed optical and IR thermal-imaging cameras. An optical high-speed video of a representative ignition is available in the Supporting Information (movie M1). Once the levitated droplet was heated by laser irradiation, the shape of the droplet started to distort. Approximately  $2 \pm 1$  ms after laser exposure, gaseous JP-10 was observed to evaporate from the surface of the droplet and heated aluminum NPs were released. The droplet ignited after  $40 \pm 5$  ms. The corresponding temperature temporal profile is displayed in Figure 3. The temperature profile shows an initial rise from 298 to  $450 \pm 24$  K, a more gradual increase to  $540 \pm 40$  K, followed by a sudden jump to a mean maximum temperature of  $2580 \pm 180$  K for an average over five ignitions. The first rise reflects the initial heating of the droplet by the laser. The final, sudden rise is caused by ignition of the droplet. After ignition, the hot surrounding gases and the explosive force caused the droplet to fall out of the trap; the sample continued to burn during the descent, while the temperature decreased as the sample was consumed. The spikes in the temperature profile are caused by heated aluminum NPs or flames randomly moving in or out of the field of view of the camera. The NP-containing droplets might ignite because, in contrast to the pure JP-10 droplets which fell out of the trap at  $452 \pm 10$  K, Al/JP-10 droplets remained trapped at temperatures of  $540 \pm 40$  K, which is higher than the autoignition temperature (509 K) of pure JP-10.

Raman spectroscopy was utilized to monitor the chemical changes during droplet ignition. Ignition of the droplet produced a black-body emission spectrum and an associated

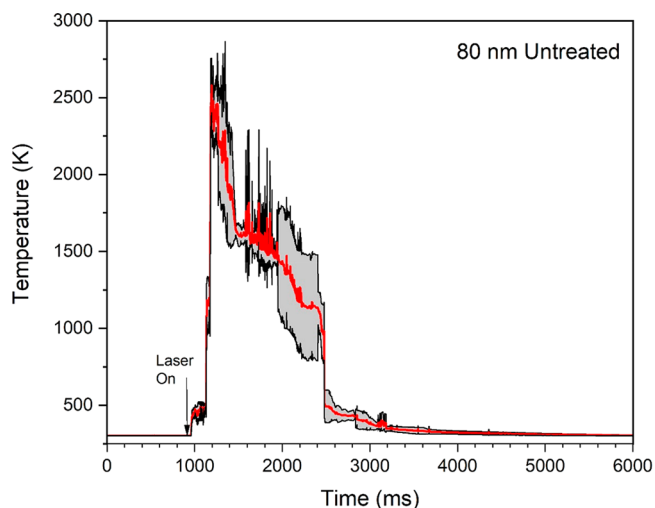


**Figure 3.** Temperature temporal profile for the oxidation of an Al/JP-10 droplet levitated in a 40% O<sub>2</sub> and 60% Ar gas mixture. The shaded area represents the range of uncertainty.

bright flash of visible light. Two new peaks occur in the Raman spectrum with apparent red shifts of  $1817 \text{ cm}^{-1}$  and  $1834 \text{ cm}^{-1}$  (Figure S4) superimposed upon the broad black-body spectrum. The peaks are produced because the black-body radiation induced atomic emission lines at 588.9 nm and 589.5 nm, which have the same wavelengths as would be produced by 532 nm photons from the excitation laser being Raman red-shifted by  $1835 \text{ cm}^{-1}$  and  $1817 \text{ cm}^{-1}$ , respectively. The emission doublet is assigned to the  $^2P_{3/2} \rightarrow ^2S_{1/2}$  and  $^2P_{1/2} \rightarrow ^2S_{1/2}$  transitions of atomic sodium at 589.00 nm and 589.59 nm, respectively.<sup>44</sup> Sodium is an inherent impurity in aluminum particles, and the atomic lines of Na have been seen previously in the combustion of aluminum.<sup>45–48</sup>

A UV–Vis spectrometer recorded the emission spectrum in the 200–1100 nm wavelength range during droplet combustion to gain further insight into the chemistry of droplet oxidation. We fitted a black-body spectrum to the UV–Vis data and obtained a mean temperature of  $2150 \pm 290$  K. The lower ignition temperature for the UV–Vis measurements compared to the value obtained by the IR thermal-imaging camera of  $2580 \pm 180$  K reflects the high sensitivity of the ignition temperature to small, unavoidable changes in the experimental conditions and the large variability in the ignition process. To display the emission peaks with improved clarity, the UV–Vis spectrum is shown in Figure 4 with the black-body spectrum subtracted in the region of special interest from 277 to 530 nm. Emissions from the OH, CH, and C<sub>2</sub> radicals are known to dominate the spectra of hydrocarbon flames and, when aluminum is present, AlO also contributes significantly.<sup>49</sup> The band centers and vibrational mode assignments for the prominent, sharper peaks in the UV–Vis emission spectra are presented in Table 1. The close agreement between the present band centers and the corresponding reference wavelengths permits the assignments to be made unambiguously. The peaks at 310 nm and 430 nm are assigned to OH ( $A^2\Sigma^+ - X^2\Pi$ ) and CH ( $A^2\Delta - X^2\Pi$ ) transitions, respectively.<sup>49</sup> The  $\Delta\nu = +1, 0,$  and  $-1$  transitions of AlO ( $A^2\Sigma^+ - X^2\Sigma^+$ ) contribute to the three bands centered at 468 nm, 487 nm, and 514 nm, respectively, where  $\Delta\nu$  denotes the change in the vibrational quantum number,  $\nu$ . The  $\Delta\nu = +1$  and 0 transitions of C<sub>2</sub> ( $A^3\Pi_g - X^3\Pi_u$ ) also contribute to the bands at 468 nm

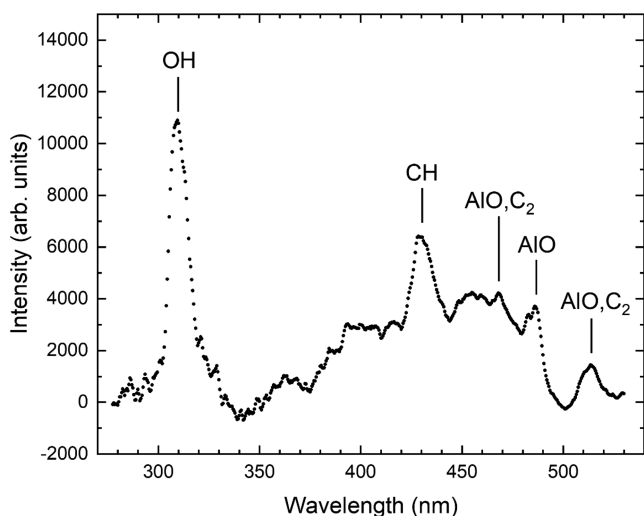


**Figure 4.** UV–Vis emission spectrum of the Al/JP-10 droplet produced by the ignition. The peak assignments are compiled in Table 1. The black-body spectrum has been subtracted.

**Table 1. Vibrational Mode Assignments of the Bands in the Emission Spectrum in the 270–530 nm Wavelength Range of JP-10 Containing 80 nm-Diameter Al Nanoparticles**

| band center <sup>a</sup><br>(nm) | molecule       | ref. wavelength <sup>b</sup><br>(nm) | transition                  | vibrational quantum numbers<br>( $\nu'$ , $\nu''$ ) |
|----------------------------------|----------------|--------------------------------------|-----------------------------|---|
| 309.8                            | OH             | 309.0                                | $A^2\Sigma^+ - X^2\Pi$      | (0, 0)  |
| 430.4                            | CH             | 431.4                                | $A^2\Delta - X^2\Pi$        | (0, 0)  |
| 468.3                            | AIO            | 467.2                                | $A^2\Sigma^+ - X^2\Sigma^+$ | (2, 1)  |
|                                  | C <sub>2</sub> | 471.5                                | $A^3\Pi_g - X^3\Pi_u$       | (2, 1)  |
| 486.7                            | AIO            | 486.6                                | $A^2\Sigma^+ - X^2\Sigma^+$ | (1, 1)  |
| 513.9                            | AIO            | 510.2                                | $A^2\Sigma^+ - X^2\Sigma^+$ | (1, 2)  |
|                                  | AIO            | 512.3                                | $A^2\Sigma^+ - X^2\Sigma^+$ | (2, 3)  |
|                                  | C <sub>2</sub> | 512.9                                | $A^3\Pi_g - X^3\Pi_u$       | (1, 1)  |
|                                  | C <sub>2</sub> | 516.5                                | $A^3\Pi_g - X^3\Pi_u$       | (0, 0)  |

<sup>a</sup>Uncertainty of  $\pm 1.0$  nm. <sup>b</sup>Reference 49.

and 514 nm, respectively. There was no evidence for emissions from atomic C, H, O, or Al across the 200–1100 nm range.

Finally, the FTIR spectrometer was used to identify the gaseous products emerging after the oxidation of the Al/JP-10 droplet (Figure 5; Table S3). These data provide evidence for the production of carbon dioxide (CO<sub>2</sub>) and water (H<sub>2</sub>O). Considering that no carbon monoxide was detected, we can conclude that molecular oxygen is the excess reactant in the oxidation of JP-10 and the aluminum NPs (Supporting Information). Bands a and b centered at 3714 cm<sup>-1</sup> and 3612 cm<sup>-1</sup>, respectively, are both produced by the  $\nu_1(\sigma_g^+) + \nu_3(\sigma_u^+)$  combination mode of carbon dioxide (CO<sub>2</sub>). Band c centered at 2349 cm<sup>-1</sup> can be attributed to the asymmetric stretching of carbon dioxide ( $\nu_3(\sigma_u^+)$ ); band e at 669 cm<sup>-1</sup> is connected to the CO<sub>2</sub> bending mode ( $\nu_2(\pi_u)$ ).<sup>50</sup> Lastly, band d is associated with water (H<sub>2</sub>O) and is assigned to OH bending ( $\nu_2(A')$ ).<sup>51</sup>

In conclusion, we explored the ignition and the oxidation of Al/JP-10 droplets levitated in an oxygen–argon atmosphere by exploiting Raman, FTIR, and UV–Vis spectroscopies along with high-speed optical and infrared thermal-imaging cameras. The identification of the diatomic radicals OH, CH, C<sub>2</sub>, and AIO from the UV–Vis emission spectra helps better understand the initial steps in the oxidation chemistry. The

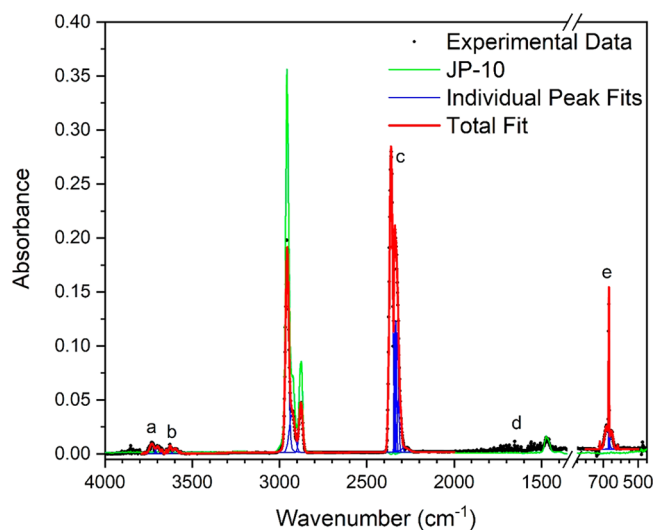


**Figure 5.** FTIR transmission spectrum after oxidation of an Al/JP-10 droplet levitated in 40% O<sub>2</sub> and 60% Ar. The product bands are labeled a–e. The wavenumbers and assignments of bands a–e are compiled in Table S3. The unlabeled bands are linked to JP-10.

addition of only 0.5 wt % of 80 nm-diameter Al NPs to JP-10 enabled ignition, which suggests that these NPs are critical in the ignition and initial chemistry of the igniting droplet. Considering that the ignition temperature of  $540 \pm 40$  K is higher than both the boiling point and autoignition temperatures of JP-10, JP-10 likely combusts before the NPs. This conclusion is consistent with previous studies on the ignition and combustion of Al/JP-10 nanofluids.<sup>24,25</sup> In the present study, the high-speed optical and IR cameras revealed that JP-10 evaporated from the surface of the droplet and heated aluminum particles were ejected from the droplet. Ignition of the JP-10 could occur via one of three possible mechanisms. The simplest mechanism involves direct laser ignition of the JP-10 vapor. In this process, the Al NPs act only to increase heat transfer from the IR laser, which enables the Al/JP-10 droplets to remain acoustically trapped as the temperature of the droplet surpasses the ignition temperature of JP-10, whereas the droplets of the pure JP-10 or droplets doped with Al<sub>2</sub>O<sub>3</sub> and CuO did not reach the boiling point before being ejected from the trap. The second oxidation mechanism involves the Al NPs acting as a catalyst. In this mechanism, the Al<sub>2</sub>O<sub>3</sub> outer shell fractures because of the heating and then the JP-10 adsorbs onto the surface of the exposed aluminum core, which possibly leads to the formation of highly reactive AlH species via hydrogen transfer reactions from a carbon–hydrogen bond of the JP-10 to the aluminum. These Al–H bonds can then be readily oxidized, as evident from the flammability of aluminum hydrides.<sup>52</sup> Furthermore, the hydrogen atom transfer from the carbon to an aluminum atom would generate carbon-centered radicals, which can be more readily oxidized than the C–H bonds of JP-10. A third potential mechanism would involve the initial oxidation of aluminum NPs. Starik et al.<sup>53</sup> and Smirnov et al.<sup>21</sup> proposed a chain mechanism for the combustion of aluminum doped *n*-decane fuels which can be applied to Al/JP-10. The oxidation is initiated by the formation of aluminum atoms in the gas phase, which react with molecular oxygen to produce highly reactive atomic oxygen and aluminum oxide (AIO)—as observed in the present study—in an exothermic reaction ( $\Delta H = -15$  kJ mol<sup>-1</sup>).<sup>54</sup> The atomic oxygen then reacts rapidly to

produce, by hydrogen abstraction from JP-10, a carbon-centered radical remaining on the JP-10 molecule along with a hydroxyl radical (OH), both of which react with other species and thus continue the chain of reaction.

Overall, the oxidation of JP-10 doped with Al NPs is a complex problem with the present work representing a first step toward a systematic elucidation of the underlying reaction pathways and mechanisms. Further experimental and theoretical studies, such as investigating the dependence of the oxidation on the aluminum particle size and droplet diameter, are clearly required to better understand these processes. Ideally, future investigations will involve pulsed femtosecond Raman and infrared spectroscopy<sup>55</sup> combined with our ultrasonic levitation apparatus to trace the initial bond rupture processes in real time and, hence, untangle whether the oxidation occurs by the carbon–hydrogen bond rupture processes followed by hydrogen transfer to the aluminum (second mechanism) or by the initial oxidation of aluminum NPs (third mechanism).

## EXPERIMENTAL METHODS

The oxidation of *exo*-tetrahydrodicyclopentadiene (JP-10) and aluminum-doped JP-10 droplets was studied using the ultrasonic levitator apparatus at the University of Hawaii at Manoa.<sup>30–33</sup> Briefly, the apparatus consists of an ultrasonic levitator enclosed in a pressure-compatible process chamber. The levitator includes a piezoelectric transducer and a concave-shaped reflector. The transducer oscillates at 58 kHz and the resulting sound wave reflects between the transducer and reflector, thereby creating a standing wave. The sound waves produce acoustic radiation pressure, which levitates a sample slightly below one of the pressure nodes of the standing wave. The droplets were injected into the levitator using a microliter droplet deposition system consisting of a syringe and needle. The Al/JP-10, Al<sub>2</sub>O<sub>3</sub>/JP-10, and CuO/JP-10 droplets were prepared by mixing 0.5 wt % of NPs with JP-10 (BOC Sciences, ≥ 98%). The Al<sub>2</sub>O<sub>3</sub> NPs (40 nm, ≥ 98%) were purchased from Skyspring Nanomaterials, Inc.; the CuO NPs (80 nm, 99%) were acquired from US Research Nanomaterials, Inc. The levitated droplets were oblate spheroids with a mean horizontal diameter of 2.7 ± 0.3 mm and a mean vertical diameter of 1.2 ± 0.3 mm. The droplets were levitated in an atmosphere containing argon (Airgas, 99.9999%), oxygen (Airgas, 99.999% purity), or an oxygen–argon mixture at a total pressure 864 Torr.

The aluminum NPs were prepared at Texas Tech University with an average diameter of 80 nm and consist of a 4 nm amorphous aluminum oxide shell surrounding an aluminum crystalline core.<sup>43</sup> Figure S5 shows transmission electron microscope (TEM) images of the powder and a single particle to illustrate the core–shell particle structure. The Al NPs were imaged using a Hitachi H-9500 TEM operating at 300 kV. To record the TEM images, the powder was suspended in ethanol, sonicated, and deposited on a Lacey Formvar film stabilized with a carbon support film, both of which are supported by 400 mesh Cu grids (Ted Pella, product no. 01885). The particle-size distribution was determined using a dynamic or static light-scattering particle-size analyzer (AccuSizer 780 SIS). Figure S6 shows the volume-weighted size distribution of the Al NPs. Roughly 25 vol % of the sample has a diameter less than 50 nm, 50 vol % is between 50 nm and 90 nm, and 25 vol % is greater than 90 nm.

The oxidation of JP-10 was monitored with Raman, Fourier-transform infrared (FTIR), and ultraviolet–visible (UV–Vis) spectroscopies. The Raman spectra were collected *in situ* using a Q-switched Nd:YAG laser emitting at a wavelength of 532 nm; the Raman-shifted photons backscattered from the droplet were collected with a HoloSpec *f*/1.8 holographic imaging spectrograph equipped with a PI-Max 2 ICCD camera from Princeton Instruments. The UV–Vis spectra were also collected *in situ* in the wavelength region of 200–1100 nm using a StellarNet SILVER-Nova UV–Vis monochromator and a fiber-optic probe. The FTIR spectra were collected in transmission mode using a Nicolet 6700 FTIR spectrometer from Thermo Scientific.

## ASSOCIATED CONTENT

### Supporting Information

The Supporting Information is available free of charge on the ACS Publications website at DOI: 10.1021/acs.jpclett.9b02241.

High-speed video of the ignition of an Al/JP-10 droplet (MP4)

Reaction yields and Figures S1–S7 and Tables S1–S3 as described in the text (PDF)

## AUTHOR INFORMATION

### Corresponding Author

\*E-mail: ralfk@hawaii.edu.

### ORCID

Stephen J. Brotton: 0000-0002-8147-2960

Michelle L. Pantoya: 0000-0003-0299-1832

Ralf I. Kaiser: 0000-0002-7233-7206

### Author Contributions

§M.L. and S.J.B. contributed equally to this work.

### Notes

The authors declare no competing financial interest.

## ACKNOWLEDGMENTS

This work was supported by the Office of Naval Research under Contract No. N000141912083. Al nanoparticle production was supported by the Office of Naval Research under Grant N00014-19-1-2082 (Texas Tech University).

## REFERENCES

- (1) Chung, H. S.; Chen, C. S. H.; Kremer, R. A.; Boulton, J. R.; Burdette, G. W. Recent Developments in High-Energy Density Liquid Hydrocarbon Fuels. *Energy Fuels* **1999**, *13*, 641–649.
- (2) Colket, M. B., III; Spadaccini, L. J. Scramjet Fuels Autoignition Study. *J. Propul. Power* **2001**, *17*, 315–323.
- (3) Osmont, A.; Gokalp, I.; Catoire, L. Evaluating Missile Fuels. *Propellants, Explos., Pyrotech.* **2006**, *31*, 343–354.
- (4) Bruno, T. J.; Huber, M. L.; Laesecke, A.; Lemmon, E. W.; Perkins, R. A. Thermochemical and Thermophysical Properties of JP-10. *2006*, *6640*, 325.
- (5) Morozov, A. N.; Mebel, A. M.; Kaiser, R. I. A Theoretical Study of Pyrolysis of *exo*-Tetrahydrodicyclopentadiene and Its Primary and Secondary Unimolecular Decomposition Products. *J. Phys. Chem. A* **2018**, *122*, 4920–4934.
- (6) Zhao, L.; Yang, T.; Kaiser, R. I.; Troy, T. P.; Xu, B.; Ahmed, M.; Alarcon, J.; Belisario-Lara, D.; Mebel, A. M.; Zhang, Y.; Cao, C.; Zou, J. A Vacuum Ultraviolet Photoionization Study on High-Temperature Decomposition of JP-10 (*exo*-Tetrahydrodicyclopentadiene). *Phys. Chem. Chem. Phys.* **2017**, *19*, 15780–15807.

- (7) Park, S. H.; Kwon, C. H.; Kim, J.; Han, J. S.; Jeong, B. H.; Han, H.; Kim, S. H. Mechanistic Insights into Oxidative Decomposition of exo-Tetrahydrodicyclopentadiene. *J. Phys. Chem. C* **2013**, *117*, 15933–15939.
- (8) Li, S. C.; Varatharajan, B.; Williams, F. A. Chemistry of JP-10 Ignition. *ALAA J.* **2001**, *39*, 2351–2356.
- (9) Parsinejad, F.; Arcari, C.; Metghalchi, H. Flame Structure and Burning Speed of JP-10 Air Mixtures. *Combust. Sci. Technol.* **2006**, *178*, 975–1000.
- (10) Gao, C. W.; Vandeputte, A. G.; Yee, N. W.; Green, W. H.; Bonomi, R. E.; Magoon, G. R.; Wong, H.-W.; Oluwole, O. O.; Lewis, D. K.; Vandewiele, N. M.; Van Geem, K. M. JP-10 Combustion Studied with Shock Tube Experiments and Modeled with Automatic Reaction Mechanism Generation. *Combust. Flame* **2015**, *162*, 3115–3129.
- (11) Vandewiele, N. M.; Magoon, G. R.; Van Geem, K. M.; Reyniers, M.-F.; Green, W. H.; Marin, G. B. Kinetic Modeling of Jet Propellant-10 Pyrolysis. *Energy Fuels* **2015**, *29*, 413–427.
- (12) Herbinet, O.; Sirjean, B.; Bounaceur, R.; Fournet, R.; Battin-Leclerc, F.; Scacchi, G.; Marquaire, P.-M. Primary Mechanism of the Thermal Decomposition of Tricyclodecane. *J. Phys. Chem. A* **2006**, *110*, 11298–11314.
- (13) Park, S. H.; Kwon, C. H.; Kim, J.; Chun, B.-H.; Kang, J. W.; Han, J. S.; Jeong, B. H.; Kim, S. H. Thermal Stability and Isomerization Mechanism of exo-Tetrahydrodicyclopentadiene: Experimental Study and Molecular Modeling. *Ind. Eng. Chem. Res.* **2010**, *49*, 8319–8324.
- (14) Xing, Y.; Fang, W.; Xie, W.; Guo, Y.; Lin, R. Thermal Cracking of JP-10 Under Pressure. *Ind. Eng. Chem. Res.* **2008**, *47*, 10034–10040.
- (15) Nageswara Rao, P.; Kunzru, D. Thermal cracking of JP-10: Kinetics and Product Distribution. *J. Anal. Appl. Pyrolysis* **2006**, *76*, 154–160.
- (16) Sun, C. J.; Sung, C. J.; Wang, H.; Law, C. K. On the Structure of Nonsmoking Counterflow Ethylene and Acetylene Diffusion Flames. *Combust. Flame* **1996**, *107*, 321–335.
- (17) Dreizin, E. L. Metal-Based Reactive Nanomaterials. *Prog. Energy Combust. Sci.* **2009**, *35*, 141–167.
- (18) Yetter, R. A.; Risha, G. A.; Son, S. F. Metal Particle Combustion and Nanotechnology. *Proc. Combust. Inst.* **2009**, *32*, 1819–1838.
- (19) Allen, C.; Mittal, G.; Sung, C.-J.; Toulson, E.; Lee, T. An Aerosol Rapid Compression Machine for Studying Energetic-Nanoparticle-Enhanced Combustion of Liquid Fuels. *Proc. Combust. Inst.* **2011**, *33*, 3367–3374.
- (20) Javed, I.; Baek, S. W.; Waheed, K. Autoignition and Combustion Characteristics of Heptane Droplets with the Addition of Aluminum Nanoparticles at Elevated Temperatures. *Combust. Flame* **2015**, *162*, 191–206.
- (21) Smirnov, V. V.; Kostritsa, S. A.; Kobtsev, V. D.; Titova, N. S.; Starik, A. M. Experimental Study of Combustion of Composite Fuel Comprising n-Decane and Aluminum Nanoparticles. *Combust. Flame* **2015**, *162*, 3554–3561.
- (22) E, X.-t.-f.; Pan, L.; Wang, F.; Wang, L.; Zhang, X.; Zou, J.-J. Al-Nanoparticle-Containing Nanofluid Fuel: Synthesis, Stability, Properties, and Propulsion Performance. *Ind. Eng. Chem. Res.* **2016**, *55*, 2738–2745.
- (23) E, X.-t.-f.; Zhang, L.; Wang, F.; Zhang, X.; Zou, J.-J. Synthesis of Aluminum Nanoparticles as Additive to Enhance Ignition and Combustion of High Energy Density Fuels. *Front. Chem. Sci. Eng.* **2018**, *12*, 358–366.
- (24) Chen, B. H.; Liu, J. Z.; Li, H. P.; Yang, W. J.; Cen, K. F. Laser Ignition and Combustion Characteristics of Al/JP-10 Nanofluid Droplet. *J. Therm. Anal. Calorim.* **2019**, *135*, 925–934.
- (25) Liu, J. Z.; Chen, B. H.; Wu, T. T.; Yang, W. J.; Zhou, J. H. Ignition and Combustion Characteristics and Agglomerate Evolution Mechanism of Aluminum in nAl/JP-10 Nanofluid Fuel. *J. Therm. Anal. Calorim.* **2019**, *137*, 1369–1379.
- (26) Liu, L.; Zhang, Q.; Shen, S.; Li, D.; Lian, Z.; Wang, Y. Evaluation of Detonation Characteristics of Aluminum/JP-10/Air Mixtures at Stoichiometric Concentrations. *Fuel* **2016**, *169*, 41–49.
- (27) Luo, Y.; Xu, X.; Zou, J.-J.; Zhang, X. Combustion of JP-10-Based Slurry with Nanosized Aluminum Additives. *J. Propul. Power* **2016**, *32*, 1167–1177.
- (28) Turns, S. R.; Wong, S. C.; Ryba, E. Combustion of Aluminum-Based Slurry Agglomerates. *Combust. Sci. Technol.* **1987**, *54*, 299–318.
- (29) Wong, S. C.; Turns, S. R. Ignition of Aluminum Slurry Droplets. *Combust. Sci. Technol.* **1987**, *52*, 221–242.
- (30) Bennett, C. J.; Brotton, S. J.; Jones, B. M.; Misra, A. K.; Sharma, S. K.; Kaiser, R. I. High-Sensitivity Raman Spectrometer To Study Pristine and Irradiated Interstellar Ice Analogs. *Anal. Chem.* **2013**, *85*, 5659–5665.
- (31) Brotton, S. J.; Kaiser, R. I. Novel High-Temperature and Pressure-Compatible Ultrasonic Levitator Apparatus Coupled to Raman and Fourier Transform Infrared Spectrometers. *Rev. Sci. Instrum.* **2013**, *84*, No. 055114.
- (32) Brotton, S. J.; Kaiser, R. I. In Situ Raman Spectroscopic Study of Gypsum ( $\text{CaSO}_4 \cdot 2\text{H}_2\text{O}$ ) and Epsomite ( $\text{MgSO}_4 \cdot 7\text{H}_2\text{O}$ ) Dehydration Utilizing an Ultrasonic Levitator. *J. Phys. Chem. Lett.* **2013**, *4*, 669–673.
- (33) Brotton, S. J.; Lucas, M.; Jensen, T. N.; Anderson, S. L.; Kaiser, R. I. Spectroscopic Study on the Intermediates and Reaction Rates in the Oxidation of Levitated Droplets of Energetic Ionic Liquids by Nitrogen Dioxide. *J. Phys. Chem. A* **2018**, *122*, 7351–7377.
- (34) Colthup, N. B.; Daly, L. H.; Wiberley, S. E. *Introduction to Infrared and Raman Spectroscopy*, 3rd ed.; Academic Press: Boston, MA, 1990.
- (35) Chen, B. H.; Liu, J. Z.; Yuan, J. F.; Zhou, J. H.; Cen, K. F. Adsorption Behaviour of Tween 85 on Nano-Aluminium Particles in Aluminium/JP-10 Suspensions. *J. Nanosci. Nanotechnol.* **2019**, *19*, 2108–2115.
- (36) Ishizuka, S.; Kimura, Y.; Kawano, J.; Escibano, R.; Yamazaki, T.; Hama, T.; Sato, R. Immiscibility of Nucleating Aluminum Oxide Nanoparticles in Vapor. *J. Phys. Chem. C* **2018**, *122*, 25092–25101.
- (37) Salehi, M.; Arabsarhangi, E. Solution Combustion Synthesis using Schiff-base Aluminum Complex Without Fuel and Optical Property Investigations of Alumina Nanoparticles. *Int. Nano Lett.* **2015**, *5*, 141–146.
- (38) Nemade, K. R.; Waghuley, S. A. Low Temperature Synthesis of Semiconducting  $\alpha\text{-Al}_2\text{O}_3$  Quantum Dots. *Ceram. Int.* **2014**, *40*, 6109–6113.
- (39) Song, X.; Fagiani, M. R.; Gewinner, S.; Schoellkopf, W.; Asmis, K. R.; Bischoff, F. A.; Berger, F.; Sauer, J. Gas-Phase Vibrational Spectroscopy of the Aluminum Oxide Anions  $(\text{Al}_2\text{O}_3)_1\text{-}6\text{AlO}_2^-$ . *ChemPhysChem* **2017**, *18*, 868–872.
- (40) Van Heijnsbergen, D.; Demyk, K.; Duncan, M.; Meijer, G.; Von Helden, G. Structure Determination of Gas Phase Aluminum Oxide Clusters. *Phys. Chem. Chem. Phys.* **2003**, *5*, 2515–2519.
- (41) Zallen, R. *The Physics of Amorphous Solids*; John Wiley & Sons: 1983.
- (42) Linstrom, P. J.; Mallard, W. G. *NIST Chemistry WebBook, Standard Reference Database Number 69*; National Institute of Standards and Technology: Gaithersburg, MD.
- (43) Gesner, J.; Pantoya, M. L.; Levitas, V. I. Effect of Oxide Shell Growth on Nano-Aluminum Thermite Propagation Rates. *Combust. Flame* **2012**, *159*, 3448–3453.
- (44) Sansonetti, J. E.; Martin, W. C. *Handbook of Basic Atomic Spectroscopic Data*; National Institute of Standards and Technology: Gaithersburg, MD, 2013.
- (45) Glumac, N.; Krier, H.; Bazyn, T.; Eyer, R. Temperature Measurements of Aluminum Particles Burning in Carbon Dioxide. *Combust. Sci. Technol.* **2005**, *177*, 485–511.
- (46) Liang, D.; Xiao, R.; Liu, J.; Wang, Y. Ignition and Heterogeneous Combustion of Aluminum Boride and Boron–Aluminum Blend. *Aerosp. Sci. Technol.* **2019**, *84*, 1081–1091.
- (47) Schloeffel, G.; Eichhorn, A.; Albers, H.; Mundt, C.; Seiler, F.; Zhang, F. The Effect of a Shock Wave on the Ignition Behavior of

Aluminum Particles in a Shock Tube. *Combust. Flame* **2010**, *157*, 446–454.

(48) Parigger, C.; Surmick, D. M.; Woods, A. C.; Donaldson, A.; Height, J. L. Measurement and Analysis of Aluminum Monoxide Flame Emission Spectra. In *8th US National Combustion Meeting*, Park City, UT, 2013.

(49) Gaydon, A. G. *The Spectroscopy of Flames*, 2nd ed.; Chapman and Hall, Halsted Press Division: London, New York, 1974; p xii, 412 P.

(50) Miller, C. E.; Brown, L. R. Near Infrared Spectroscopy of Carbon Dioxide I.  $^{16}\text{O}^{12}\text{C}^{16}\text{O}$  Line Positions. *J. Mol. Spectrosc.* **2004**, *228*, 329–354.

(51) Max, J.-J.; Chapados, C. Isotope Effects in Liquid Water by Infrared Spectroscopy. *J. Chem. Phys.* **2002**, *116*, 4626–4642.

(52) Urben, P. *Bretherick's Handbook of Reactive Chemical Hazards*; Elsevier: 2017.

(53) Starik, A. M.; Kuleshov, P. S.; Sharipov, A. S.; Titova, N. S. Kinetics of Ignition and Combustion in the Al-CH<sub>4</sub>-O<sub>2</sub> System. *Energy Fuels* **2014**, *28*, 6579–6588.

(54) Honma, K.; Miyashita, K.; Matsumoto, Y. Reaction Dynamics of Al + O<sub>2</sub> → AlO + O Studied by a Crossed-Beam Velocity Map Imaging Technique: Vib-Rotational State Selected Angular-Kinetic Energy Distribution. *J. Chem. Phys.* **2014**, *140*, 214304.

(55) Kobayashi, T.; Du, J. Femtosecond Real-Time Vibrational Spectroscopy using Ultrafast Laser Pulses. *Ser. Opt. Photonics* **2013**, *8*, 1–28.